small methods
www.small-methods.com

Direct Visualization and Identification of Membrane Voltage-Gated Sodium Channels from Human iPSC-Derived Neurons by Multiple Imaging and Light Enhanced Spectroscopy

Manola Moretti, Tania Limongi, Claudia Testi, Edoardo Milanetti, Maria Teresa De Angelis, Elvira I. Parrotta, Stefania Scalise, Gianluca Santamaria, Marco Allione, Sergei Lopatin, Bruno Torre, Peng Zhang, Monica Marini, Gerardo Perozziello, Patrizio Candeloro, Candido Fabrizio Pirri, Giancarlo Ruocco, Giovanni Cuda, and Enzo Di Fabrizio**

In this study, transmission electron microscopy, atomic force microscopy, and surface enhanced Raman spectroscopy are combined through a direct imaging approach, to gather structural and chemical information of complex molecular systems such as ion channels in their original plasma membrane. Customized microfabricated sample holder allows to characterize Na_v channels embedded in the original plasma membrane extracted from neuronal cells that are derived from healthy human induced pluripotent stem cells. The identification of the channels is accomplished by using two different approaches, one of them widely used in cryogenic electron microscopy (the particle analysis method) and the other based on a novel Zernike Polynomial expansion of the images bitmap. This approach allows to carry out a whole series of investigations, one complementary to the other, on the same sample, preserving its state as close as possible to the original membrane configuration.

1. Introduction

Ion channels are membrane proteins playing a crucial role in cell growth and proliferation, neurotransmission, heart and muscle contraction, immune response, and water balance. Due to their broad distribution in cells and their critical role in physiological and pathological processes, ion channels represent important and potential targets for drug discovery and pharmacological safety. They have been associated with different genetic diseases, referred as channelopathies, some of which account for genetic human epilepsies.[1–6] Although the characterization of plasma membranes and ion channels

M. Moretti, M. Allione, B. Torre, P. Zhang
King Abdullah University of Science and Technology
SMILEs lab, PSE Division, Thuwal 23955-6900, Kingdom of Saudi Arabia
E-mail: manola.moretti@kaust.edu.sa

T. Limongi, M. Marini, C. F. Pirri, E. Di Fabrizio
Dipartimento di Scienza Applicata e Tecnologia
Politecnico di Torino
Corso Duca Degli Abruzzi 24, 10129 Torino, Italy
E-mail: enzo.difabrizio@polito.it

C. Testi, E. Milanetti
Center for Life Nanoscience
Istituto Italiano di Tecnologia
Viale Regina Elena 291, 00161 Rome, Italy

The ORCID identification number(s) for the author(s) of this article can be found under https://doi.org/10.1002/smtd.202200402.

DOI: 10.1002/smtd.202200402

E. Milanetti, G. Ruocco
Department of Physics
Sapienza University
Piazzale Aldo Moro 5, Rome 00185, Italy

M. T. De Angelis, E. I. Parrotta, S. Scalise, G. Santamaria, G. Cuda
Laboratory of Stem Cell Biology
Department of Experimental and Clinical Medicine
University Magna Graecia
Campus S. Venuta, Viale Europa, Catanzaro 88100, Italy

S. Lopatin
King Abdullah University of Science and Technology
Imaging and Characterization Core lab
Thuwal 23955-6900, Kingdom of Saudi Arabia

G. Perozziello, P. Candeloro
BionNEM lab and Nanotechnology Research Center
Department of Experimental and Clinical Medicine
University Magna Graecia
Campus S. Venuta, Viale Europa, Catanzaro 88100, Italy

transport has been deeply studied[7–9] and theoretical models have been developed, detailed multiple imaging approaches and characterization of the cell membrane by high-resolution techniques are still missing.[10–14] Furthermore, the direct visualization of single ion channels in their native plasma membrane will significantly help to improve our understanding of the pathophysiology of ion channels and prompt innovative research in drug screening and precision medicine.

Voltage-gated sodium (Na_v) channels mainly act as molecular triggers of action potentials in neurons, skeletal muscle as well as in other excitable cells. Protein subunits of these channels, identified in 1980 by Beneski and Catterall,[15] are represented by a 260 kDa α subunit containing the voltage sensors and the ion-conducting pore, associated with auxiliary 30–40 kDa β subunits (β1- β4)[16] involved in kinetics and voltage-dependence modulation. Four distinct α subunits, namely Na_v1.1, Na_v1.2, Na_v1.3, and Na_v1.6, are expressed in the central nervous system. Each of these subunits is encoded by a specific gene (*SCN1A*, *SCN2A*, *SCN3A*, and *SCN8A*, respectively). More than 600 mutations have been identified in the *SCN1A* gene, most of which have been linked to genetically inherited epilepsy syndromes. Other groups reported significant advancements in the understanding of the structure and functional states of the Na_v channel,[17] describing in a very thorough manner its voltage sensing, activation, conductance, fast and slow inactivation.[18]

In the present study, we aimed at localizing and identifying the Na_v channels directly on a suspended plasma membrane patch by using two distinct high-resolution imaging approaches, Transmission Electron Microscopy (TEM) and Atomic Force Microscopy (AFM), and combine them with Enhanced Raman spectroscopy analysis for getting further information on the secondary structure of the channel. Starting from a method proposed by our group,[19–25] a new sample preparation protocol was optimized. Cell membranes were extracted from neurons differentiated from neural stem cells (NSCs) derived from human induced pluripotent stem cells (hiPSC) generated from a healthy donor. Membranes' patches were suspended on a super-hydrophobic surface (SHS) characterized by an alternation of holes and microfabricated micropillars, ready to be investigated. The identification of the channels of interest was afterwards successfully performed by the use of a new algorithm based on Zernike polynomials expansion of the image bitmap combined with single particle analysis. Single particle analysis is routinely adopted to reconstruct the 3D structure of proteins from cryo-EM images. Usually, the sample, e.g., the protein of interest, is isolated from the cellular environment via purification processes and embedded in a thin layer of ice; if a membrane protein is analyzed, it must be also included in a lipid bilayer support, such as a lipid nanodisc.[26–28] Apart from the significant challenge of achieving successful purification steps for high resolution cryo-EM imaging,[29,30] the sample preparation adopted so far for imaging membrane proteins does not allow to preserve the original milieu, thus possibly hindering important information. Notwithstanding, the very well established single particle analysis software was successfully applied to identify the channels studied in this work, thus providing a benchmark for the validation of our data collection method and the data analysis based on Zernike polynomial expansion.

Finally, we would highlight how inserting an immunogold labeling step among the sample preparation methods, allowed us both to precisely identify the Na_v channels by TEM and to obtain valuable information on their secondary structure by Surface Enhanced Raman Spectroscopy (SERS). Surface Enhanced Raman signal originates from an enhancement in the electric field at the surface when the incident light on the sample excites localized surface plasmons. Several noble metals, 2D materials and 3D nanostructures are in use to provide enhanced Raman signal for biomolecules detection.[31–36] Gold nanoparticles immune labeling was previously applied to target tumors,[37] specific cell membrane molecules[38,39] etc., however this combinatorial approach has not been used before. Conversely, the mechanical properties, in terms of local plasticity, related to the transmembrane protein assembling characteristics retrieved from stiffness and damping AFM measurements, correlated to the shift of the Raman band related to the strain state of the ion channel protein configuration.

The method we present in this paper aims to assist researchers and clinicians by providing the possibility of carrying out, on a single sample, a whole series of morphological, structural and compositional characterization of single ion channels in their native membrane. It could significantly contribute to elucidate the phenotype induced by a severe genetic disease and the effect of specific drug targeting, therefore becoming a suitable analytical method in a patient specific platform. Furthermore, it could be particularly useful in the case of low sample availability or when the retrieval of samples requires invasive procedures and it is consequently recommended to minimize the number of withdrawals to ensure the safety and comfort of the patient.

2. Results and Discussion

The sample preparation method used in this work is based on the effect of a droplet evaporation on a super-hydrophobic patterned surface (SHS).[21] After the isolation procedure, plasma membranes are resuspended in a suitable buffer and deposited on the SHS. During the evaporation of the sample, the droplet decreases its volume shrinking back from the external pillars toward the center of the device and the membrane patches, with a surface area in the range of tens of micron squares, are suspended between the pillars after complete evaporation. The suspended membrane portions are stable both in air and in vacuum, thus allowing TEM (**Figure 1**a) and AFM (**Figure 2**a) characterization together with Raman spectroscopy analysis (**Figure 3**a).

2.1. TEM Imaging of Suspended Neuron Membranes

We started the characterization by performing direct imaging of the Na_v channel with a FEI Titan TEM operating at 300 keV acceleration voltage (Figure 1; Figure S1, Supporting Information). The SEM micrograph in Figure 1b reveals the presence of membrane patches suspended on top of the pillars' matrix. The dark feature in the middle of Figure 1b is the microfabricated hole allowing the free passage of TEM electrons, as shown schematically in Figure 1a. In Figure 1c high magnification of several membrane channels are visible as highly contrasted spots.

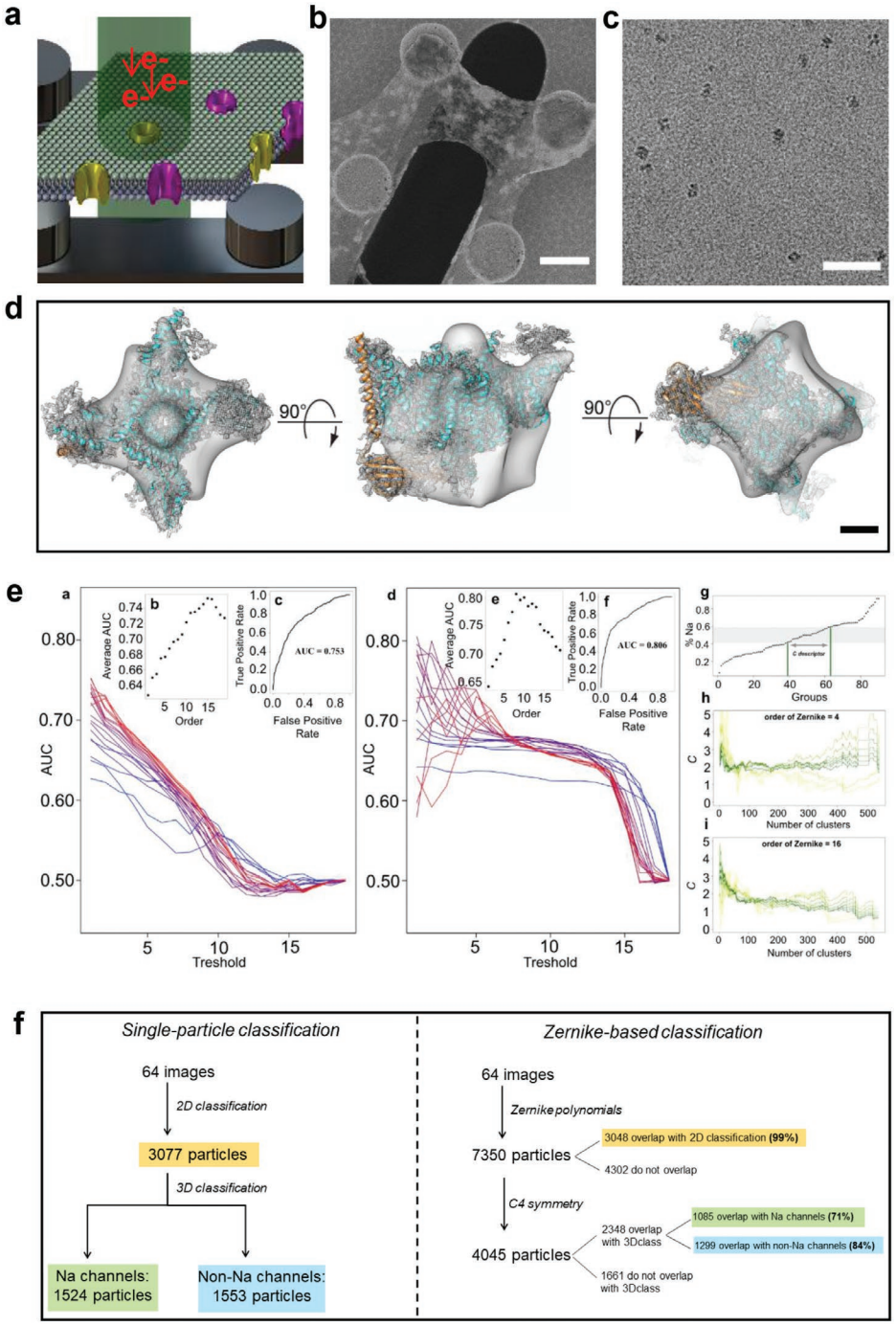

Figure 1. TEM imaging of the Na_v channel, single particle analysis by RELION and Zernike polynomial results. a) Sketch of the sample characterization method where the plasma membrane suspended across the SHS is investigated by TEM. b) SEM micrograph of the neuronal plasma membrane suspended over the SHS. Scale bar 4 µm. c) TEM image of the suspended neuronal membrane where different ion channels can be localized (darker spots). Scale bar 30 nm. d) Final postprocessing map (solid grey volume) at 14.4 Å resolution overlapped to the PDB structure of human Nav1.4 (PDB code 6AGF,[16] cyan and orange) and its cryo-EM map (EMDB 9617, fine grey mash; this map has been strongly filtered using the "hide dust" feature in Chimera, in order to hide the noisy contribution of lipid nanodiscs). In orange, the β1 subunit. Scale bar = 20 Å. e) Results obtained by comparing the method based on Zernike polynomials and the standard procedure based on RELION. a) AUC of the ROC as a function of the threshold, i.e., be the number of neighbors. The color is in accordance with the expansion order, where blue indicates low order and red indicates high order. b) The average value of the AUC of the ROC as the order of expansion varies. c) The ROC curve corresponding to the best case: d–f) These are the same results described in (a,b,c) normalizing the data in Z-score. g) Definition of the C descriptor, which is based on the Na channels percentage in the ordered classification of the groups identified with clustering analysis. h,i) C descriptor as a function of the number of clusters considered for two orders of expansion ($N = 4$ and $N = 16$). The color is in accordance with the number of neighbors, from yellow to green. f) 2D FFT of the TEM image in (f) final results comparison between single particle classification based on RELION and Zernike-based classification.

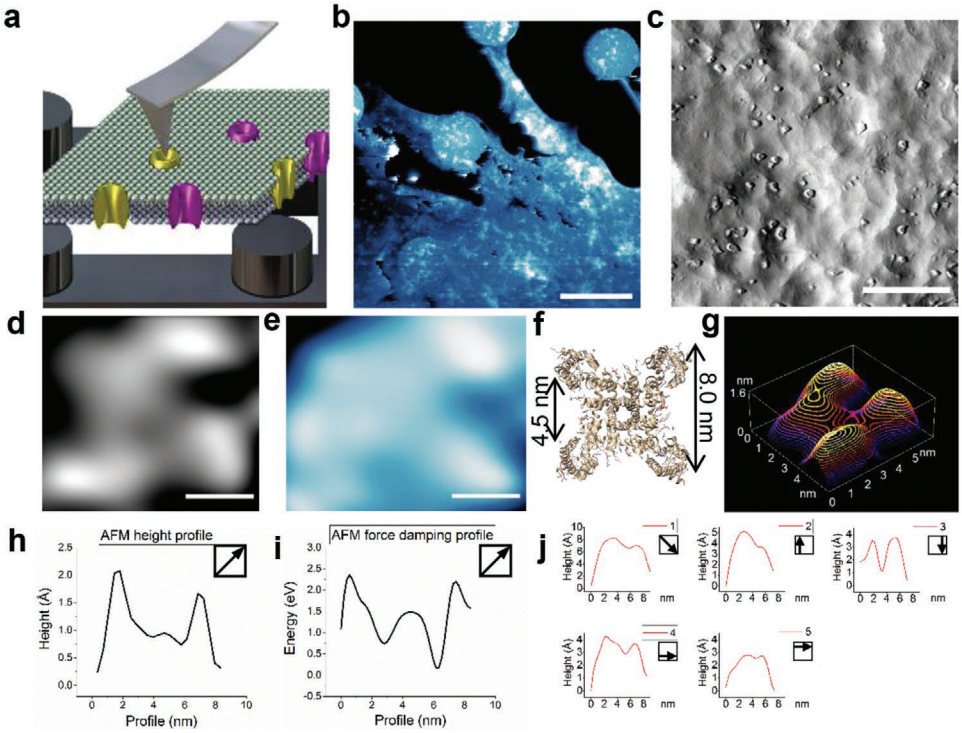

Figure 2. AFM imaging of the Na_v channel. a) Sketch of the sample characterization method where the suspended plasma membrane is investigated by AFM. b) AFM height topography of a large area of the suspended neuronal plasma membrane over the SHS. Scale bar 5 µm. c) AFM amplitude signal of the suspended neuronal membrane where different features can be localized. Scale bar 100 nm. d,e) AFM height topography and AFM force damping map of a single Na_v channel respectively. Scale bar 2 nm. f) Molecular graphic plotted with Chimera of the Na_v channel according to PDB file 5EK0 with inner and outer lengths indicated. g) 3D surface plot of topography in d, with isolines of 1 Å step size. h,i) AFM height diagonal profile and AFM force damping diagonal profile of the contrast $\Delta E_{protein}$ of the putative Na_v channel, of respectively (d) and (e). j) Profiles drawn in the AFM topography image in d, where the arrows in the inset squares indicate the position and direction of each plotted profile.

2.1.1. Single Particle Analysis

To solve the structure of Na_v channels, we collected 126 frames and performed single-particle analysis using RELION (Figure 1c; Figure S2, Supporting Information).[40] The average classes resulting from the reference-free 2D classification routine (Figure S3a, Supporting Information) show some lateral views of the channels, whose features are in accordance with other high-resolution 2D classifications available in literature.[26,41–43] Since the membranes are not perfectly flat suspended, in some locations they are not perpendicular to the TEM beam and consequently, even a lateral view of the channel is possible. These properties avoid preferred proteins orientation and allow for many different Euler angles to be imaged, thus possibly obtaining a complete three-dimensional (3D) reconstruction by single-particle algorithms.[44,45] Taking advantage of this fact, with just 126 frames we obtained a 3D map of Na_v channels (Figure 1d). We used a strongly low-pass filtered structure of human $Na_v1.4$ (PDB code 6AGF,[16] the only structure so far available in literature as belonging to a human Na_v channel) as reference model, resulting in a final map of 14.4 Å resolution as calculated by Fourier Shell Correlation curve (Figure S3b, Supporting Information). We then overlapped our resulting map to the high-resolution cryo-EM (EMDB 9617) and its derived PDB structure, shown in Figure 1d. Although at a lower resolution, our map largely overlaps the cryo-EM one obtained by lipid nanodiscs that, albeit largely exploited for cryo-EM imaging of membrane proteins, might alter their native environment.[46,47]

As such, we can conclude that the sample preparation method described in this work might be successfully used in combination with single-particle analysis in order to obtain high-resolution 3D maps of membrane proteins in their native environment, possibly overcoming demanding purification procedures that might contribute to generate artefacts altering their physiological structural properties. In addition the multiple channels present in the natural membrane, can all be analysed in a single preparation. Moreover, even if at this stage the resolution obtained is quite modest, higher resolution TEM images can be obtained in the future.

2.1.2. Channel Classification Comparison Based on Zernike Polynomials

Here, we also present a novel computational procedure able to automatically identify channels from experimental frames obtained by TEM imaging, discriminating Na_v channels among others with good accuracy. A portion of the image bitmap of size comparable to- (but slightly larger than-) the channel dimension is thought as a 2D single-valued surface, sampled on a regular lattice (the image pixels), where the "color" (a 8 or 14 bits binary number) represents the value of the function $f(x,y)$ at the pixel

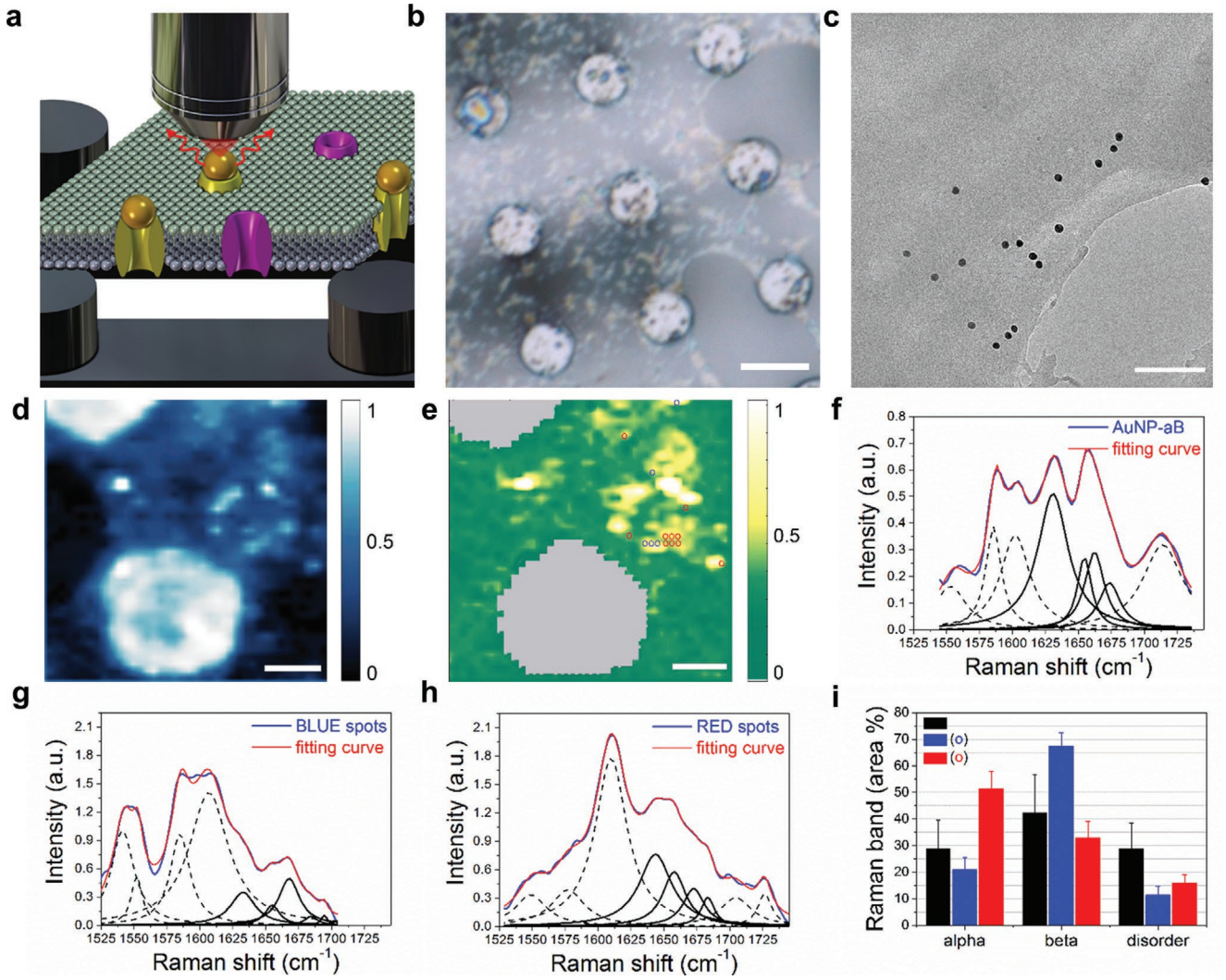

Figure 3. Raman spectroscopy of the immunogold labeled SCN1a subunit of the Na_v channel on the suspended neuronal membrane. a) Sketch of the Raman spectroscopy imaging setup, where a single Na_v channel, specifically tagged with a gold nanoparticle, is imaged. b) Optical image of a portion of the suspended neuronal membrane on the SHS. Scale bar 5 µm. c) TEM image of the neuronal membrane with gold nanoparticles tagging specifically the SCN1a subunit by immuno-labeling. Scale bar 100 nm. f–h) Raman measurements (blue curve), fitting curves (red), and specific single curves used to describe the secondary structure regions in the Amide I range (full black) for the gold nanoparticles with covalently linked antibody (AuNP-aB), and for the immuno-gold construct tagging the Na_v channels in different docking regions, indicated as blue and red spots in e, respectively (for an explanation of dotted lines fitting curves see methods). d) Optical signal arising from the nano-gold construct on the suspended neuronal membrane. Scale bar 2 µm. e, Raman spectroscopy imaging. The intensity color scale relates to the area in the range of 1500–1750 cm^{-1} (Amide I region): blue and red circles indicate the 2 sub-populations in g and h, according to PCA analysis. Scale bar 2 µm. i) Histogram of fitting results relative to α, β, and disordered secondary structures in the Amide I region for the red spots spectra (red), blue spots spectra (blue), and reference gold nanoparticles antibody tagged spectra (black).

location x,y. In order to compare different image patches, and to identify the kind of channel found in the patches, we performed a polynomial expansion of the function $f(x,y)$. The coefficients of the polynomial expansion -here we use the Zernike polynomials- are thus a "representation" of the channel shape, the more accurate the more extended is the polynomials set. In order to compare different channels, we more easily compare the coefficients, which do not depend either on the orientation or on the translation of the image. Therefore, there is no need to apply a time-consuming images rototranslation to find the best matches. The comparison of the expansion coefficients directly gives information on the degree of similarity of two images.

Indeed, the single particle analysis used above may suffer from the reduced dimensionality of the dataset: so, we developed a new and independent image classification method of the same micrographs to corroborate the 2D and 3D classifications found by RELION. The advantages of this new approach, with respect to standard characterization methods, are both the need of low computational times and the fact that the procedure is automated. Furthermore, it is a completely parameter and reference-free approach that not requires a large number of frames to obtain more reliable results. The method is based on the shape characterization of each channel via a series expansion in the 2-D Zernike basis. Each particle was associated to

a set of Zernike coefficients and the particles were then compared among each other and with the RELION analysis. In particular, the RELION classification was used to identify the particles associated or not to the Na_v channels among the results from Zernike descriptions of the same particles. Afterwards, a population of particles described by similar Zernike coefficients was classified as Na_v channels, based again on RELION classification. The procedure for the identification, extrapolation and characterization of each channel is reported in the Experimental Section.

Additionally, we tested the ability of the method to find clusters mainly composed of Na_v channels by using the 3D classification obtained from RELION providing two groups of channels, namely dividing Na_v channels from the rest of the channels (Na_v and non-Na_v). To this end, for each identified channel, we selected a set of neighbouring channels as defined by the distance between the vectors composed of Zernike coefficients (see the Experimental Section). For each group of neighbours we calculated the percentage of Na_v channels to determine the nature of each selected channel based on its comparison with the most similar channels in terms of shape properties.

We studied the performance of the method to correctly classify Na_v channels measuring the area under curve (AUC) of the Receiver Operating Characteristic (ROC) curve, ranging from 0.5 (completely random classification) to 1 (perfect classification) (Figure 1e).

For the proposed analysis, over the total 126 frames, we only considered a subset of 64 images characterized by higher contrast. On these images the algorithm automatically found 7350 channels, 3048 of which were in overlap with those selected by the 2D Classification procedure of RELION, which finds 3077 channels (Figure 1f).

Among these channels, we selected only those with a high C4 symmetry level-characteristic of Na_v channels-as calculated by adding the contributions of specific Zernike coefficients Zc4 (see the Experimental Section). More in detail, we selected the channels for which the C4 symmetry value was greater than the average of all values, obtaining 4045 channels. Among these, 1085 and 1299 were Na_v and non- Na_v channels identified with single-particle analysis (Figure 1f). To perform a quantitative analysis, each channel was associated with an invariant under rotations set of Zernike coefficients, meaning that the orientation of each channel did not affect the comparison with any other. In such a way, the computationally extensive alignment procedure of single-particle analysis was avoided.

The two methods largely overlapped in finding the same particles as belonging to the same groups (Figure 1f).

We studied the AUC of the method as the order of expansion and the number of neighbours vary (see Figure 1e). The number of first neighbours was selected step by step as the distance threshold changes, ensuring that the minimum number of first neighbours was 5. The optimal value of the expansion order of the Zernike polynomials, for which we obtained a maximum of the performance (AUC = 0.753), was $N = 16$ (see Figure 1e). On the other hand, when z-score normalization was used for this comparison, we find the best matching between the two approaches resulted an AUC of the ROC of 0.806 corresponding to the expansion order $N = 9$ (see Figure 1e).

In Figure 1e we show that the performance of the Na_v channel classification is maximum for a small number of selected neighbours. A further analysis was conducted to investigate the best number of channel subgroups. A clustering analysis was performed at each expansion order of the Zernike polynomials, from 2 to 20. For each order, the descriptor C was calculated (see the Experimental Section for its definition) providing information about the optimal separation between the two groups of channels: "Na_v" and "non-Na_v". The lower the descriptor C, the greater the discrimination between the two groups. The analysis showed that, approximately, the best number of groups to separate the Na_v channels from the non-Na_v ones is, considering the order $N = 16$, in the range from 100 to 200 (see Figure 1e).

Starting from these results, which demonstrate the method's ability to determine Na_v channels considering the nature of the channels most similar in shape, we can associate with a channel (putative Na_v channel due to its proximity to an antibody tagged gold nanoparticle, Figure S4, Supporting Information) a set of similar channels (first neighbours), which will be predicted, with a high probability, to be Na_v channels too. Three channels known to be Na_v channels, have been experimentally identified by immunogold labeling (further details in the chapter on Raman spectroscopy) and, for each of these, we identified the set of channels, which are the most similar in terms of Zernike descriptors. The percentage of the predicted Na_v channels depends on the numbers of neighbours we select for each of the three Na_v channels, which were previously identified with the nanoparticle. For the three channels identified we found a maximum percentage of Na_v channels of 0.78, 0.62, and 0.89, in the range of neighbours between 10 and 20 channels with data normalized by Z score transformation.

Differentiated cells derived from human induced Pluripotent Stem Cells hiPSC cells have distinguished expression signatures than the ones derived from human Embryonic Stem Cells (hESC).[48] In particular, for what concerns the expression levels of ion channels in the cell membranes of hiPSC derived neurons, a decrease in expression levels of about 15% has been reported,[49] and transcriptome data analysis consistently report on a different morphology, neuronal activity and expression levels of several genes in hiPSC.[50,51] Distribution of ion channels, in neurons particularly, is not homogeneous and can be highly compartmentalized.[52] Single molecule tracking has previously shown that Na_v channels are mostly present at the neurite ends, and in the cell's body organize in clusters.[53] In this context, the authors observed 4–5 nanoclusters containing 2–20 ion channels per 1 μm^2. In our analysis by RELION and Zernike polynomials, we quantified the Na_v channels to be about 1085/20 μm^2, therefore resulting roughly in 51 channels per μm^2, which matches significantly the results, reported from single particle tracking analysis.

2.2. AFM Imaging of Suspended Neuron Membranes

After TEM characterization, the same sample was further investigated by AFM to obtain a detailed topographic map providing additional 3D structural insights on the channels embedded in their native membrane (Figure 2). In Figure 2b, the AFM topography performed on a large area of the sample, allowed to identify the pillars and the membrane patches. The amplitude AFM signal of an area of roughly 2 by 2 µm scan (Figure 2c), reveals a densely populated surface where features

of the size of ion channels (around 10 nm diameter) and even smaller features were displayed. In Figure S5 in the Supporting Information we report on how also these images reveal several morphological features. Among these, we identified what resembles the ion channel observed in the TEM imaging as in Figure 1d. By comparing the TEM and the AFM images with their channel profile plots (Figure S6 in the Supporting Information with Figure 2h,j), the two techniques revealed size accordance between the features, where the AFM topography along the diagonal profile resulted in having 7.6±0.5 nm size (Figure 1h). In order to better appreciate the 3D information provided by the AFM measurement, a 3D surface plot was generated (Figure 2g). Rendering isolines with step size of 1 Å showed a full height range of 5.7±0.3 Å. Additionally, several height profiles related to the Figure 2d are reported: these are respectively shown as diagonal profiles in Figure 2h,j (n. 1) and as longitudinal profiles of the sides of the squared channel in Figure 2j (n. 2–5). The diagonal profiles mean value was 7.6±0.5 nm. The average of the side profiles numbers 3, 4 and of numbers 5, 6 measured 5.1±0.5 nm and 6.4±0.5 nm respectively. As can be noted the profile lengths that are in the slow scanning direction of the AFM probe appear to be smaller, due to the thermal drift of the sample.[54] This artifact accounts for the smaller size of the Na_v channel found in the AFM image when compared to the TEM data (Figure S6, Supporting Information). Overall, the metrology derived from both the TEM and AFM images is compatible with the whole sizes derived from the PDB file 5EK0[55] (Figure 2f), keeping in mind that a slight difference can be attributed to the embedding of the channel in its native environment and to TEM imaging limited contrast and AFM thermal drift effect. Additional information on the mechanical and structural properties of the ion channel was retrieved by analyzing the mechanical interaction between the AFM probe and the membrane's surface during imaging (Figure 2e,i). Here we used the approach proposed by Garcia et al.,[56] by combining the mechanical properties of the cantilever and the amplitude and the phase images to compute a map of the dissipative tip-sample interaction, therefore providing a quantitative measurement of the local plasticity of the area investigated (Figure 2e). A similar approach was used by Stark et al.[57] to provide a quantitative interpretation of the phase images of the trimers of bacteriorhodopsin in purple membrane supported on mica substrates, and later by Santos et al.[58] to directly measure the energy dissipation on supported DNA in different interaction regimes, demonstrating the reliability of using the energy quantification to identify different measurements regimes, their impact on the resolution and the role of the substrate. A quantitative energy loss map was obtained for the Na_v channel (Figure 2e) and compared with its topography (Figure 2d). The measurement of the damping depends on the stiffness and compliance[59] local variations, and therefore allows a direct access to quantities determining the biomechanics under the surface of the protein. The damping values that we found in correspondence to the protein, range from 125 to 127.5 eV and are compatible with those deduced from Stark et al.[57] and Santos et al.,[58] when we rescale for the oscillatory parameters. While the full diagonal dimension is conserved between the height and damping map profiles (compare the values in Figure 2h,i), the contrast in the protein region $\Delta E_{protein}$ = 2.5 eV (Figure 2e) showed a breaking of the four-fold symmetry of the Na_v channel, if compared with AFM height topography and TEM images (Figure 2d; Figure S6b, Supporting Information), revealing a more complex organization of the underneath structure. This was also confirmed by the band shift relative to α-helix and by the disordered structure bands measured in the SERS experiments (data available not shown here). Although at this time we do not have available Na_v channel identification for the AFM imaging, we are confident that immune-gold labeling will provide adequate support as for the previous chapter.

2.3. Raman Spectroscopy on Suspended Neuron Membranes

Finally, Raman spectroscopy measurement was performed by combining immunogold labeling and SERS (Figure 3; Figure S7, Supporting Information). This approach was successfully used before, where SERS was applied to obtain specific antigen/antibody recognition in solution.[60] The use of 10 nm gold nanoparticles, functionalized with the specific antibody for the Na_v channel $Na_v1.1$ subunit was designed for two main reasons. On one side, the antibody functionalization of the nanoparticle allowed the specific docking to a subunit of the Na_v channel, thus the recognition of the channel for further analysis by Zernike-based classification. On the other side, the gold nanoparticle worked as a plasmonic enhancer for the subsequent Raman analysis leading to SERS effect only in the proximity of the ion channel. The literature reports about a plasmonic effect developing to a distance of about 6–10 nm when the gold nanoparticle is 10 nm diameter.[61] The size of an antibody is roughly 4–5 nm in solution, therefore it is reasonable to expect a contribution deriving from the Na_v channel when the docking has occurred. Moreover, we cannot exclude the contribution of a gap-mode configuration of two or more nanoparticles electromagnetic field.[62] Therefore, Raman spectroscopy accomplishes the conformational channels determination by providing essential information on the chemical composition and on the structural organization of the Na_v channel. Using our superhydrophobic devices for the membrane suspension (Figure 3b,c), we clearly revealed information on the secondary structure of the proteins forming the ion channels. Due to the synergy of the specific docking and the SERS effect, we detected the Raman signal scattered out only from the nearby of the Na_v channel (Figure 3d,e). Where the nano-gold construct was not present and hence no enhancement was acting (darker color in the optical map in Figure 3d), the membrane scattering showed a usually poor signal-to-noise ratio. SERS data were further analyzed by Principal Component Analysis (PCA), which led to classify SERS hot-spots in two main groups, labeled with red and blue circles on the Raman map (Figure 3e; Figure S8, Supporting Information). Multiparametric fitting in the Amide I frequency range[63] (see the Experimental Section) of both red and blue averaged spectra provided an evaluation of α-helix, β-sheet, and disordered structures ratios (Figure 3g,h). According to fitting results (Figure 3i), the blue circles on the map were β-sheet dominant, while the red ones were predominantly α-helix sites. A comparison with SERS measurements performed only on gold antibody-functionalized nanoparticles

(Figure 3f) showed that the spectral behavior of the blue spots closely resembles the antibody in terms of secondary structure composition, being mainly β-sheet (Figure 3i). On the other hand, the red spots clearly deviated from the antibody behavior, showing a major component of α-helix structure. We suggest that the red spots related spectra are a clear contribution from the Na_v channel, due to the specific docking of the gold nanoparticles. In fact, from the analysis of the secondary structures composition from the histogram related to the red spots (Figure 3i), after excluding the percentage related to the antibody (β-sheet = 35%), we estimated a percentage of 72% of α-helix and 28% of disordered structures. These values are in good agreement with the literature, which reports 69% of α-helix and 31% of disordered structures for the whole Na_v channel.[55]

3. Conclusion

This analysis provides the first visualization and characterization, to our knowledge, of the Na_v channels from hiPSC-NSCs, by a combination of TEM, AFM, and SERS techniques. Our approach holds enormous potential in terms of biomedical applications. Mutations affecting the *SCN1A* gene are, in fact, responsible for several channelopathies. Although detailed structural information of this multi-subunit protein is available, a high-resolution multi-technique description of the channel is still lacking, making it difficult to draw reliable conclusions on genotype/phenotype correlations in patients bearing such mutations.

We are presently using the integrated approach described above to analyze hiPSC-NSCs from a family with an inherited form of febrile seizures secondary to a specific *SCN1A* gene mutation.[64] We aim to dissect the molecular mechanisms underlying the disease and to bring novel information on the structural changes produced by this mutation on the morphology of the nuclear channel.[64,65] Besides other important applications, this method can be extended to other channelopathies involving nervous, cardiovascular, respiratory, urinary systems that may arise as a consequence of ion channel defects. Together with this multiple characterization approach we also present a new theoretical-computational method with the aim of identifying the Na_v channel among the many particles found in the TEM imaging frames. The ability of the method to discriminate Na_v channels from non-Na_v channels was tested by comparison with the classification obtained with the standard single particle analysis based on RELION. The new procedure proposed here has several advantages: it is efficient and fast, it is completely parameter and reference free, and the comparison between two or more channels is easily feasible since the characterization method is based on rotational invariant descriptors. The approach also shows a greater ability to detect channels, increasing the statistics and the possibility of finding biologically relevant channels. Even though preliminary, the findings described here represent an innovative and original strategy for the direct visualization, at high resolution, of important protein complexes involved in critical physiological and pathological processes. This approach will be particularly useful when healthy and diseased patients will be screened since, by preparing a single sample, it is possible to make several characterizations taking a smaller quantity of sample, which is desirable in the case of bone marrow punctures or liquid biopsies. As future outcomes of the present approach, we expect important insights in the study of channel docking mechanism and of targeting protein-channel interfaces for the modulation/reactivation of membrane ion channels in pathology or in in vitro/in vivo drug delivery tests.

Finally, this investigation methodology can, in principle, be conducted in solution for the study of the time dynamical response of the opening/closing of the Na_v channel both for wild type and mutated channels, and has the potential to be compatible with membrane studies with the well-established electrophysiological methods.

4. Experimental Section

Generation of Human Induced Pluripotent Stem Cells (hiPSCs): A skin biopsy specimen from a healthy donor was obtained after written informed consent. All consenting procedures were done under institutional review by the board of the ethical committee of the University Magna Græcia of Catanzaro. Fibroblasts were isolated from dermal biopsy by the outgrowth method and expanded in DMEM with 10% Fetal Bovine Serum (FBS, Thermo Fisher Scientific), 50 U mL^{-1} penicillin, and 50 µg mL^{-1} streptomycin. Reprogramming of skin fibroblasts to pluripotency was carried out by non-integrating Sendai-virus-mediated (CytoTune-iPS 2.0 Sendai Reprogramming Kit, Thermo Fisher Scientific) transduction of the four canonical transcription factors (*OCT4*, *SOX2*, *KLF4*, and *c-MYC*) in feeder-independent conditions on Matrigel-coated dishes (90-120 µg mL^{-1}, BD Biosciences) in mTeSR1 medium (STEMCELL Technologies) (**Figure 4**a). Pluripotency was verified by microarray data analysed by PluriTest algorithm[66,67] and by immunostaining (Figure 4b). Following cell fixation with 4% (vol/vol) paraformaldehyde (PFA) for 15 min, the cells were rinsed 3 times with phosphate-buffered saline (PBS), permeabilized with PBS with 0.5% Triton X-100 (Sigma) and blocked with 10% (vol/vol) normal goat serum (NGS; Vector) for 1 h at room temperature (RT). The following primary antibodies were used: human NANOG (1:1000; rabbit polyclonal, Abcam), human OCT4 (1:400; mouse monoclonal, STEMCELL Technologies). Subsequently, cells were incubated with Alexa Fluor-647, -594, and -488 conjugated secondary antibodies (all from Life Technologies) for 1 h at 37 °C. Nuclei detection was obtained labeling cells with 1 µg mL^{-1} DAPI (Thermo Fischer Scientific). Microscope slides were mounted with Dako Fluorescent Mounting Medium and cells were inspected by DMi8 microscope setup (Leica Microsystems) (Figure 4b,d).

Generation of Human Induced Pluripotent Stem Cells (hiPSCs)—Induction of Neural Stem Cells (NSCs): For differentiation into NSCs, hiPSCs at 15–25% confluency were cultured with Neural Induction Medium (Thermo Fisher Scientific) for 7 days. After that, 1×10^5 cells per cm^2 cells were plated on Geltrex-coated dishes (120-180 µg mL^{-1}, Thermo Fisher Scientific) and cultured in Neural Expansion Medium until ready for maturation (Figure 4c).

Generation of Human Induced Pluripotent Stem Cells (hiPSCs)—Neuronal Differentiation of hiPSC-Derived NSCs: hiPSC-derived NSCs were dissociated with StemPro Accutase (Thermo Fisher Scientific) and 5×10^4 cells per cm^2 were re-suspended in Neuronal Differentiation Medium with CultureOne Supplement on Poly-D-Lysine (10 µg mL^{-1}, Sigma, P6407) and laminin (3 µg mL^{-1}, Gibco, 23 017 015)-coated plates (Figure 4c). Differentiated hiPSC-derived neurons were kept in this condition for 5 weeks for maturation.

Generation of Human Induced Pluripotent Stem Cells (hiPSCs)—Plasma Membrane Isolation: Cells were rinsed twice in ice-cold 1 × phosphate-buffered saline (PBS), and directly lysed in the culture dish by adding an hypotonic buffer solution (0.32 M sucrose, 5 mM Hepes, 1 mM EDTA,

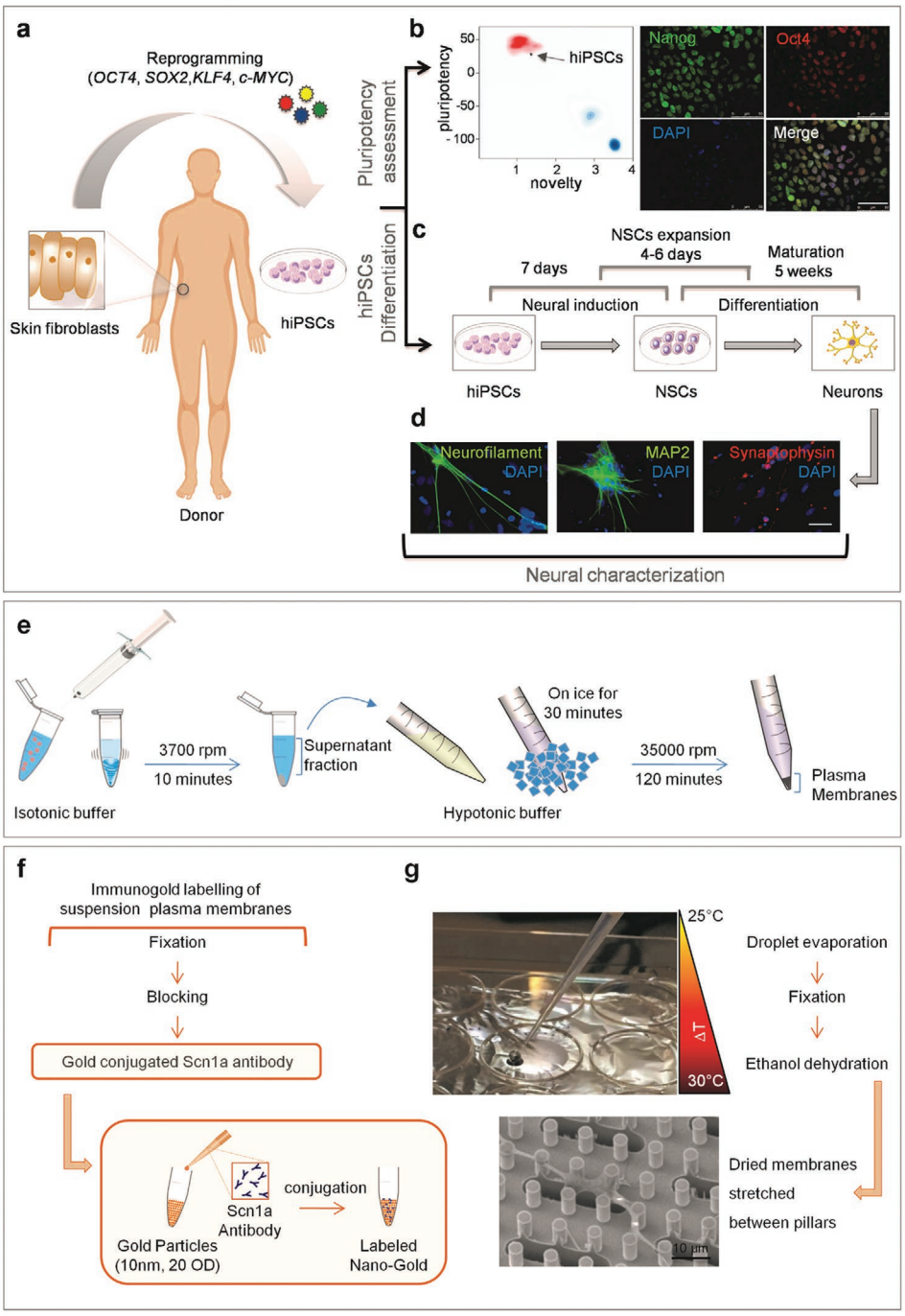

Figure 4. Overview of the experimental procedure used in this study. a) Reprogramming strategy: dermal fibroblasts from a healthy individual were isolated from a skin biopsy and reprogrammed into hiPSCs using Sendai viruses coding for OCT4, SOX2, KLF4, and c-MYC. b) PluriTest analysis of hiPSCs (black circle) with a high "pluripotency score" and a low "novelty score" indicating that they resemble normal human pluripotent stem cells (in red). Immunofluorescence analysis of pluripotency markers NANOG (green) and OCT4 (red) in a representative iPSC clone. Nuclei were counterstained with DAPI (blue). Scale bar, 50 µm. c) hiPCS-derived neurons were obtained using the PSC Neural Induction and Differentiation kit. hiPSCs grown in feeder-free condition were first coaxed to differentiate into neural stem cells (NSCs) that were expanded for 4–6 days before differentiation (at passage 1) into Neurons. Five weeks-old neurons were used for further analysis. d) Immunofluorescence analysis of mature neuronal-associated markers Neurofilament (green), MAP2 (green) and Synaptophysin (red). Nuclei were counterstained with DAPI (blue). Scale bar, 50 µm. e) Basic steps of plasma membrane isolation from hiPSCs-derived neurons after 5 weeks of maturation. f) Flowchart of plasma membrane suspension labeling with gold conjugated-SCN1a antibody procedure. The conjugation reaction occurred by the interaction of lysine residues of the purified antibody to the gold particles surface. g) On the left, deposition of membrane sample droplet on SHS placed on a plate whose temperature is 5 °C higher than room temperature (RT). On the right, scheme of treatment after droplet evaporation process. Below, the SEM image of neuronal membranes suspended on the pillars of the SHS device.

pH 7.4). Cell lysates were passed several times through syringe needles gauge 21 and then vortexed thoroughly for 1 min to homogenize. The homogenized lysates were centrifuged at 3000*g* for 10 min at 4 °C to pellet nuclei, whole cells, and large cellular debris. The supernatant fraction was diluted 10 times with hypotonic buffer solution (5 mM Hepes, 1 mM EDTA, pH 7.4), homogenized by vortexing for 2 min, and kept on ice for 30 min. After the last centrifugation at 35 000 rpm for 120 min at 4 °C, the supernatant was discarded and membrane pellets were re-dissolved in hypotonic buffer solution (schematics in Figure 4e).

Generation of Human Induced Pluripotent Stem Cells (hiPSCs)—Immunogold Labeling and Deposition on SHS: This step was carried out on membranes in suspension (Figure 4f). Following fixation with 4% PFA for 15 min, samples were rinsed three times with PBS and once with 50 mM glycine for 30 min. After 30 min blocking with PBS containing 3% BSA (Bovine Serum Albumin Fraction V, Sigma-Aldrich), samples were incubated with gold conjugated Na_v 1.1 (gene *SCN1A*) antibody (Abcam, ab24820) in 0.1% BSA overnight at 4 °C. The antibody was conjugated with gold nanoparticles following manufacturer's instructions of GOLD Conjugation Kit (10 nm 20OD) (Abcam, ab201808). Gold-stained membranes pellet were re-suspended in H_2O after several washing steps to remove unbounded antibody. After incubation, samples underwent to a centrifugation step (15 000 rpm for 5 min) after which the supernatant was discarded. 10 µl drops were deposited on SHS and let dry on a hot plate with a temperature set 5 °C higher than the RT (Figure 4g). Then the samples were fixed using 1.2% glutaraldehyde in 0.1 M cacodylate buffer (pH 7.4) for 1 h, and washed three times with 0.1 M cacodylate buffer, and later three times with ice-cold Milli-Q water. Finally, samples were dehydrated by rinsing them for 5 min in an increasing series of ice-cold ethanol (25%, 35%, 50%, 70%, 80%, 90%, 96% and thereafter 100% two times). Before being processed with AFM and TEM, samples were kept in a dry environment to preserve their integrity.

Device Fabrication: The micropillared substrate was fabricated according to previous reports[22,23,68] by standard lithographic technique procedures. The process is detailed in the Supplementary information.

TEM Imaging: Bright-field TEM images were acquired on a Titan 60-300 transmission electron microscope (FEI) equipped with a high-brightness electron gun (x-FEG), a spherical aberration (CS) corrector of the imaging part of the objective lens, and Gatan K2-IS high-speed direct detection camera. The microscope was operated at 300 keV acceleration voltage. With a defocus range of 2–3 microns TEM images were acquired as series of 40 frames with 0.1 s per frame rate and post-acquisition drift correction frame integration was applied. Thus, images were acquired with a total exposure time of 4 sec (40 frames per image). Electron beam intensity was adjusted to result in the exposure rate of about 12–15 electrons per pix s^{-1}, and the average total dose of 20 electrons per Å∧2 on the specimen plane.

Image processing for SI was carried out as follows: the image of the channel of interest was extracted by FFT and inverse FFT processing in a single image. Then, the pixel size of the image was increased 4 times and Gaussian smoothing was performed with a 2-pixels size. For the purpose of plotting, 1-pixel thick profiles of the original image were extracted and B-spline interpolated with a fixed resolution of 50, whereas for the values reported in the main text, the profiles were extracted from the original image.

Images were compared with the PDB file 5EK0 of the Na_v channel.[55] Graphics and measurements on this molecule were performed by using the Chimera software.[69]

Single-Particle Data Analysis of TEM Images: We collected 126 micrographs. Frames were aligned for beam-induced motion correction using the embedded software Gatan. global contrast transfer function was calculated using Gctf.[70] All subsequent single-particle data analysis was carried out using RELION 3.1.[40]

1200 particles were manually picked to produce a reference for the automated particle picking procedure implemented in RELION. These particles were used to create the first reference-free 2D classes. A total of 23 241 particles were automatically picked and extracted from the original micrographs.

After the extraction, particles were subjected to 2D classification in two rounds, using K = 25 classes and regularization parameter T = 2. These class averages show the channels as seen from different orientations (Figure S3a, Supporting Information).

Particles belonging to good classes (6202 particles) were subjected to 3D classification, using K = 8 classes, C4 symmetry and T = 4. As a reference model for classification, we used a strongly low-pass filtered (60 Å) PDB structure of $Na_v1.4$ containing Beta1 (PDB code 6AGF[16] transformed in electron density map by using CHIMERA[69] "molmap" command. We did not use the corresponding cryo-EM model (EMDB 9617[16]) because of the strong noise of lipid nanodiscs in the deposited structure that, when low-pass filtered, completely altered the 3D structure of the map. Good particles (3078) resembling the Na channel structure were selected for refinement using the 3D Autorefine procedure and the same map as 3D classification. A subset of these particles was also used for Zernike comparison. Final masking, using a soft-edge mask of 5 pixels, and PostProcessing gave an overall resolution of 14.4 Å (Figure S3b, Supporting Information). The resolution of the map was estimated with the Fourier shell correlation (FSC) = 0.143 criterion, based on the "gold-standard" protocol.[71–73]

UCSF Chimera was used for graphical visualizations of the electron density maps and crystallographic structures.

Single-Particle Data Analysis of TEM Images—2D Zernike Polynomials and Invariant Descriptors: A bi-dimensional image can be described by a two variables function, which is expressed in polar coordinates. This function can be defined inside a unitary circle and then decomposed in the Zernike basis as follows

$$f(r,\Phi) = \sum_{n=0}^{\infty}\sum_{m=0}^{m=n} C_{nm} Z_{nm}(r,\Phi) \tag{1}$$

where $C_{nm}$are the expansion coefficients, while the complex functions, $Z_{nm}(r,\varphi)$ are the Zernike polynomials.

More specifically, theC_{nm}coefficients are defined as

$$C_{nm} = \frac{(n+1)}{\pi}\langle Z_{nm} \mid f\rangle = \frac{n+1}{\pi}\int_0^1 dr r \int_0^{2\pi} d\phi Z'_{nm}(r,\phi) f(r,\phi) \tag{2}$$

Each polynomial can be divided into two parts: a radial ($R_{nm}(r)$) and an angular ($e^{im\varphi}$) part

$$Z_{nm} = R(r) e^{im\phi} \tag{3}$$

where the radial part for any n and m, is given by

$$R_{nm}(r) = \sum_{k=0}^{\frac{n-m}{2}} (-1)^k \frac{(n-k)!}{k!\left(\frac{n+m}{2}-k\right)!\left(\frac{n-m}{2}-k\right)!} r^{n-2k} \tag{4}$$

The complete set of polynomials forms a basis, given that

$$\langle Z_{nm} \mid Z_{n'm'}\rangle = \frac{\pi}{(n+1)}\delta_{nm'}\delta_{nm'} \tag{5}$$

The knowledge of the set of complex coefficients, C_{nm}, allows for a univocal reconstruction of the original image, whose resolution depends on the expansion order *N*.

Single-Particle Data Analysis of TEM Images—Computational Procedure for Channel Identification: The purpose of this procedure is to identify, extrapolate and characterize each channel belonging to an image obtained from the experimental procedure.

Each image of the dataset, which is saved in "tiff" format, is read by the R software through the "readTIFF" function, meaning that the values of the pixels are integer numbers ranging from 0 to 255. We call this starting image *Mat* (follow the entire procedure in **Figure 5**).

Starting from the *Mat* matrix, other two matrices are obtained, *RhoMat* and *RhoMatIm*, smoothing the initial one by replacing the value

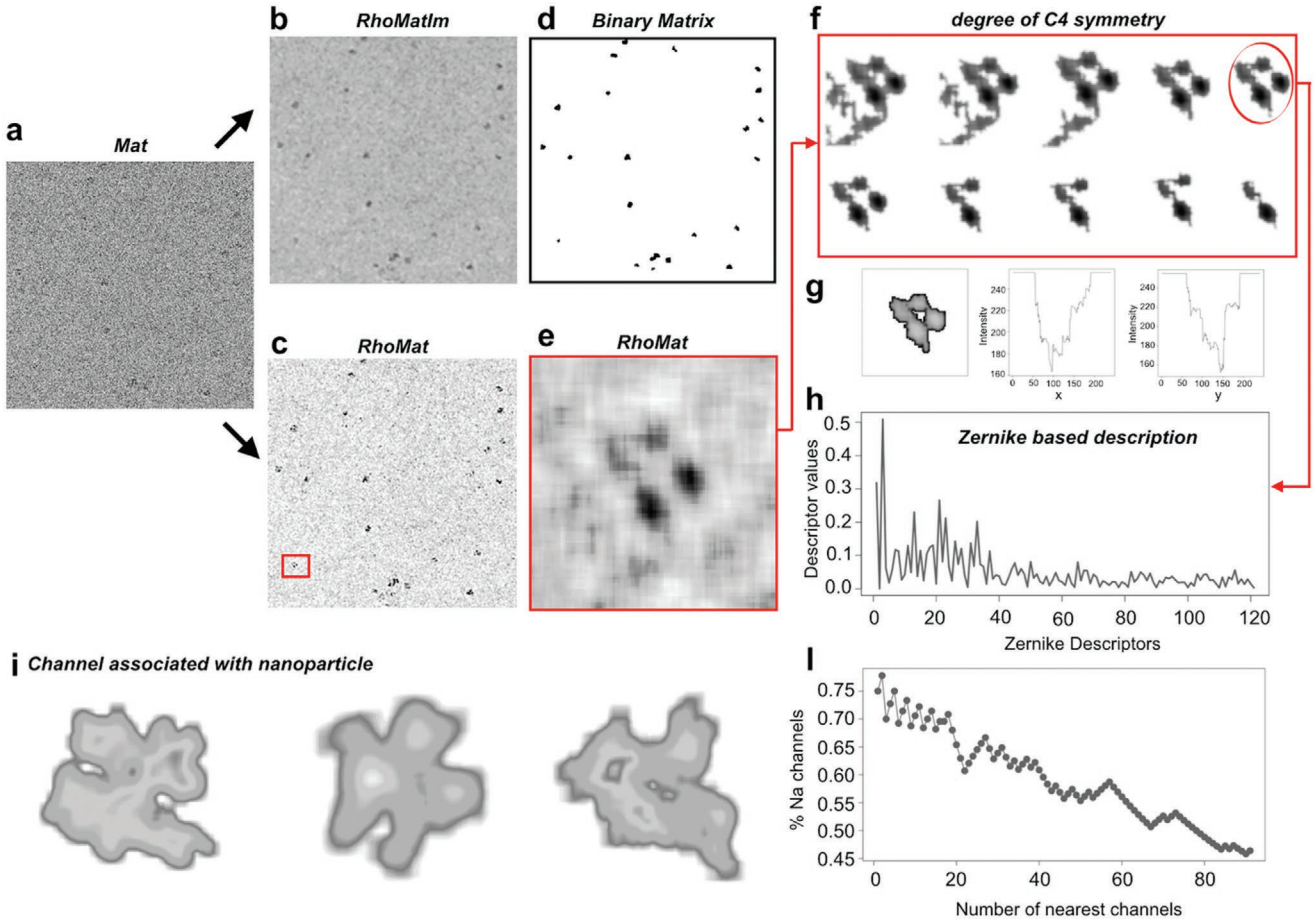

Figure 5. Protocol of the computational procedure for the selection and characterization of channels. a) Mat: starting matrix as obtained from the experimental procedure. b,c) RhoMatIm and RhoMat are two matrices obtained from the Mat matrix considering two smooth procedures which use a side of 5 and 10 pixels for RhoMat and RhoMatIm respectively. d) Binary matrix, where for each matrix element there is 0 or 1 according to a threshold value. e) Zoom of the RhoMat matrix to better view a given channel. f) Several representations of the same channel for different thresholds of the index that measure the degree of C4 symmetry. g) Channel selection considering the cut-off value that maximizes the symmetry C4. The mean of the intensities both along the *x* and along the *y* is also shown. h) Zernike invariant descriptors considering the twentieth order of expansion. i) Graphic representation (through an appropriate smoothing procedure) of the three Na channels, experimentally identified through the nanoparticles. l) Percentage of Na channels as the number of neighbour's varies (in terms of Zernike vectors) for the first channel of (i).

of each pixel *i* with the average of the pixels belonging to a square of side L centered in *i* (where L values are: $L_{Mat} = 5$LMat = 5 and $L_{MatIm} = 10$ for *RhoMat* and *RhoMatIm* respectively).

The *RhoMatIm* matrix is used to identify the regions where every single channel takes place. As the first step, the *RhoMatIm* matrix is binarized, meaning that each pixel value is replaced with 0 or 1 values according to a fixed threshold value. To optimize the binarization process, here we defined as $C_{nm} = \overline{P} - \alpha * \sigma_p$, where $\overline{P}$ the mean of all values and p the corresponding standard deviation. Here we choose $\alpha = 1.8$.

A clustering analysis is performed in order to identify the clusters composed only by no null pixels. To this end *hclust* function of R package with single algorithm andnhattan distance is used.[74]

Since many identified clusters are characterized by a size too small, these certainly cannot be defined as membrane channels, but rather they are due to noise. For this reason, we only select objects with a pixel count greater than 150 and lower than 2000 (in order not to include regions that represent image artifacts).

Each identified cluster is mapped to the *RhoMat* matrix. In order to centered the channel in a rectangular box, we add l pixels both along the *x* and *y* directions of the original image. In this case we set l = 25, starting from the pixels with higher and lower *x* (as well as pixels with higher and lower *y*). Let's name the rectangular where the single channel is centered Ri.

To extract the object from its context and treat it alone, we need to select a cutoff, under which each pixel is assigned the null value and above which we keep the assigned value. This cutoff must be chosen appropriately so as not to add noise portions of the entire matrix, but also not to remove important regions of the selected channel. To this end we select a threshold value for each channel maximizing the C4 symmetry of the analyzed object.

This is possible using the description based on Zernike polynomials because specific invariant descriptors are null if they describe an object with perfect C4 symmetry (Zc4). Indeed, the periodicity of the trigonometric functions implies invariance under rotation by multiples of 2mradian around the center of the image

$$Z_{nm}\left(r,\theta+\frac{2\pi k}{m}\right)=Z_{nm}(r,\theta) \tag{6}$$

Exploiting this property, we can select the best cut-off for each object by minimizing the sum of the coefficients which should be zero for an image with C4 symmetry. This allows us to use an optimal cut-off for each identified object in such a way as to make it as C4 as possible.

In some cases, the selected object is mainly composed of noise (or image background), which are high contrast regions that do not represent a channel. Therefore, we remove these objects by imposing that the percentage of constantly null values both along the rows and the columns are less than 0.85 and greater than 0.15.

Single-Particle Data Analysis of TEM Images—Channel Classification: The remaining candidate channels are described by a set of coefficients of the Zernike polynomials, allowing us to compare each pair of channels in terms of their shape. Here, we use the cosine metric to calculate the distance between two Zernike coefficient vectors *a* and *b*

$$\mathrm{Dis} = 1 - \frac{\sum_{i=1}^{n} a_i b_i}{\sqrt{\sum_{i=1}^{n} b_i^2}\sqrt{\sum_{i=1}^{n} a_i^2}} \tag{7}$$

A clustering analysis was performed among the Zernike vectors using the *hclust* function of the *stat* library of R with the "ward.D" algorithm.[75]

To evaluate the goodness of the classification of the two groups of channels obtained from the clustering procedure, we calculate the descriptor C as follows: we sort the clusters from the one with the lowest to the one with the highest percentage of Na channels. If the cluster perfectly divides the two categories of channels (Na and non-Na) into two groups, the descriptor C is a step function. Therefore, by setting a range of values of the Na channels percentage, we define the descriptor C as

$$C = \frac{N_{gr}}{N_g\,(p_u - p_l)} \tag{8}$$

where N_{gr} is the number of groups belonging to the percentage range, N_g is the total number of groups, p_u and p_l the upper and lower percentage for which N_{gr} is calculated. We vary this range by considering from a minimum value of 0.4 to a maximum value of 0.6.

AFM Imaging: The same sample containing the neuronal membrane of interest, previously imaged with the TEM, was measured in a JPK Nanowizard III AFM mounted on inverted Olympus IX73. AFM imaging was performed in tapping mode using XSC11AlBS cantilevers (Mikromasch, GmbH), with the cantilever free oscillation at~120 kHz frequency and a spring constant of 4.25 N m^{-1}. Scan size was maintained at 2×2 μm^2 sampling at 2048 points per line, with the probe running at 0.1 Hz rate. The measurements were performed by keeping the sample at less than 15% Rh. Data analysis was performed with the proprietary JPK software and Gwyddion software,[76] if not otherwise indicated. Image processing was carried out by scaling the area of interest by a factor of 10 and with a Gaussian smoothing of size 2 pixels. Profiles were extracted from the original image. 3D surface plots were generated by using ImageJ[77] interactive 3D surface plot, applying a grid size of 256 pixel and a smoothing on 10 pixel. Calculation of energy dissipation was performed according to Garcia et al.,[56] by combining the amplitude A_{SP} and phase ϕ images acquired during tapping topography measurements, after accurate calibration of the free cantilever spring constant k (4.25 N m^{-1}), quality factor Q (253) and free oscillation amplitude (20 nm) according to the following formula

$$E_L = \left(\sin\varnothing - \frac{A_{SP}}{A_0}\right)\frac{A_{SP}}{A_0}E_0 \tag{9}$$

where

$$E_0 = \pi k A_0^2 / Q \tag{10}$$

Is the mechanical energy of the free oscillating cantilever.

Raman Spectroscopy: Raman spectroscopy was performed on a sample previously labeled with antibody conjugated gold nanoparticles, specifically tagging the SCN1a subunit of the Na_v channel (Figure S1, Supporting Information). The sample was excited with a HeNe laser with linearly polarized output at 632.8 nm wavelength and 0.5 mW power, while a confocal Raman spectrometer (Alpha 300 RA, Witec) equipped with an Andor CCD camera (DU970N thermoelectrically cooled at -65 °C) was used to analyze and record the spectra. The sample was measured in confocal backscattered geometry through a 100x objective (Zeiss, Ec Epiplan Neofluar, 0.9 NA). Raman spectroscopy maps of 10×10 µm and 40×40 points were acquired at 0.5 seconds integration time per point. PCA analysis of the spectra dataset was performed in order to identify hotspots of SERS signals containing information on the secondary structure of the ion channel. The scores of first principal component PC1 discriminate the spectra of hot spots of Figure 3e in two sub-populations, which are labeled with red and blue circles (Figure S8, Supporting Information). Average spectra of the two subpopulations are then analysed by multiparametric fitting (Figure 3g,h). For data comparison, Raman spectra on antibody conjugated gold nanoparticles were also acquired. The Amide I signal, from the C = O stretching vibration of the protein backbone, was considered for the evaluation of the percentage of the secondary structure components. Multi-parametric fitting in the Amide I frequency range was performed according to.[63] Briefly, fitting to mix Lorentzian-Gaussian curves was performed after baseline subtraction and normalization to the integrated intensity of the spectra. The χ^2 value of the fitting defined the choice of the number of peaks to fit in the range of 1500–1750 cm^{-1}. In this case, several peaks were incorporated in the fitting: three in the range of 1515–1615 cm^{-1} related to aromatic amino acids side chain residues, one peak at 1640 cm^{-1} that we experimentally related to the water component of the suspended membrane, three peaks in the ranges of 1650–55 cm^{-1} (α-helix), 1665–70 cm^{-1} (β-sheet), 1675–85 cm^{-1} (disordered structures), and one or two peaks in the range of 1690–1730 cm^{-1} assigned in the literature to $\nu(CO_2^-)$ stretches in proteins.[78] In the case of the Raman map images, values were extracted integrating the spectral intensity in the range of 600–1000 and 1500–1750 cm^{-1} to reveal the nano-gold construct optical signal and the presence of protein secondary structure, respectively.

Statistical Analysis: Since several methods for statistical analysis were adopted according to the technique used, details on the methodology for data analysis is reported in each specific paragraph.

Supporting Information

Supporting Information is available from the Wiley Online Library or from the author.

Acknowledgements

The authors acknowledge financial support from King Abdullah University of Science and Technology for OCRF-2014-CRG and OCRF-2016-CRG grants; SHAHEEN cluster to provide machine time; Professor Charlotte A. E. Hauser for providing access to SHAHEEN, and from Piedmont Region through European Funds for Regional Development ("Food Digital Monitoring" project); European Research Council Synergy grant ASTRA (n. 855923). The abstract has been updated on July 20th 2022 after initial online publication.

Conflict of Interest

The authors declare no conflict of interest.

Author Contributions

M.M. performed the AFM and Raman spectroscopy measurements and data analysis, conceived the SERS imaging together with Enzo Di Fabrizio, and significantly contributed to the writing of the MS; T.L.

conceived the experiment with Enzo Di Fabrizio, contributed in image editing and in writing the MS; C.T. performed the image analysis with relion and wrote part of the manuscript; E.M. performed the analysis with Zernike polynomials method and wrote part of the manuscript; M.T.D.A., E.P., S.S., and G.S. performed the cell biology part, including the plasma membrane extraction and membrane deposition on the SHS and contributed in writing the MS; M.A. planned and fabricated the micro-structured SHS device; S.L. performed the TEM measurements and advised on TEM image analysis; B.T. advised on the whole AFM imaging experimental part, analyzed AFM data and contributed to the writing of the MS; P.Z. made the image sketches depicting the device working principle in this MS; M.M. optimized the dilution condition for the membrane deposition on the SHS and contributed to the writing of the MS; G.P. and P.C. performed the Raman spectroscopy data analysis and contributed to the writing of the MS; C.F.P. contributed to the writing the MS and discussed the multiple technique approach; G.R. conceived the data analysis with the combination of Relion and Zernike polynomials and wrote part of the manuscript; G.C. supervised the cell biology part of the work and contributed to the writing of the MS; E.D.F. conceived and supervised the work, organized the collaborators, and wrote the MS.

Data Availability Statement

The data that support the findings of this study are available from the corresponding author upon reasonable request.

Keywords

AFM, Raman spectroscopy, superhydrophobic surfaces, TEM, voltage gated sodium channels, Zernike polynomial

Received: March 30, 2022
Revised: April 22, 2022
Published online: May 20, 2022

[1] A. Moreau, M. Chahine, *Front. Cardiovasc. Med.* **2018**, *5*, 139.
[2] H. Corvol, S. M. Blackman, P. Y. Boelle, P. J. Gallins, R. G. Pace, J. R. Stonebraker, F. J. Accurso, A. Clement, J. M. Collaco, H. Dang, A. T. Dang, A. Franca, J. Gong, L. Guillot, K. Keenan, W. Li, F. Lin, M. V. Patrone, K. S. Raraigh, L. Sun, Y. H. Zhou, W. K. O'Neal, M. K. Sontag, H. Levy, P. R. Durie, J. M. Rommens, M. L. Drumm, F. A. Wright, L. J. Strug, G. R. Cutting, et al., *Nat. Commun.* **2015**, *6*, 8382.
[3] S. Behere, S. Weindling, *Ann. Pediatr. Cardiol.* **2015**, *8*, 210.
[4] A. Fernández-Falgueras, G. Sarquella-Brugada, J. Brugada, R. Brugada, O. Campuzano, *Biology* **2017**, *6*, 7.
[5] J. Spillane, D. M. Kullmann, M. G. Hanna, *J. Neur. Neurosurg. Psychiatry* **2016**, *87*, 37.
[6] M. Vaeth, S. Feske, *Curr. Opin. Immunol.* **2018**, *52*, 39.
[7] A. Hirano-Iwata, Y. Ishinari, H. Yamamoto, M. Niwano, *Chem. Asian J.* **2015**, *10*, 1266.
[8] E. Neher, B. Sakmann, *Nature* **1976**, *260*, 799.
[9] R. Kawano, Y. Tsuji, K. Sato, T. Osaki, K. Kamiya, M. Hirano, T. Ide, N. Miki, S. Takeuchi, *Sci. Rep.* **2013**, *3*, 1995.
[10] H. Subramanian, A. Froese, P. Jonsson, H. Schmidt, J. Gorelik, V. O. Nikolaev, *Nat. Commun.* **2018**, *9*, 2446.
[11] P. Novak, J. Gorelik, U. Vivekananda, A. I. Shevchuk, Y. S. Ermolyuk, R. J. Bailey, A. J. Bushby, G. W. Moss, D. A. Rusakov, D. Klenerman, D. M. Kullmann, K. E. Volynski, Y. E. Korchev, *Neuron* **2013**, *79*, 1067.
[12] Y. F. Dufrene, T. Ando, R. Garcia, D. Alsteens, D. Martinez-Martin, A. Engel, C. Gerber, D. J. Muller, *Nat. Nanotechnol.* **2017**, *12*, 295.
[13] P. R. Laskowski, M. Pfreundschuh, M. Stauffer, Z. Ucurum, D. Fotiadis, D. J. Muller, *ACS Nano* **2017**, *11*, 8292.
[14] Y. E. Korchev, Y. A. Negulyaev, C. R. W. Edwards, I. Vodyanoy, M. J. Lab, *Nat. Cell Biol.* **2000**, *2*, 616.
[15] D. A. Beneski, W. A. Catterall, *Proc. Natl. Acad. Sci.* **1980**, *77*, 639.
[16] X. Pan, Z. Li, Q. Zhou, H. Shen, K. Wu, X. Huang, J. Chen, J. Zhang, X. Zhu, J. Lei, W. Xiong, H. Gong, B. Xiao, N. Yan, *Science* **2018**, *362*, 6412.
[17] J. Payandeh, T. Scheuer, N. Zheng, W. A. Catterall, *Nature* **2011**, *475*, 353.
[18] W. A. Catterall, *Exp. Physiol.* **2014**, *99*, 35.
[19] M. Marini, A. Falqui, M. Moretti, T. Limongi, M. Allione, A. Genovese, S. Lopatin, L. Tirinato, G. Das, B. Torre, A. Giugni, F. Gentile, P. Candeloro, E. Di Fabrizio, *Sci. Adv.* **2015**, *1*, 1500734.
[20] T. Limongi, F. Cesca, F. Gentile, R. Marotta, R. Ruffilli, A. Barberis, M. Dal Maschio, E. M. Petrini, S. Santoriello, F. Benfenati, E. Di Fabrizio, *Small* **2013**, *9*, 402.
[21] M. Marini, T. Limongi, A. Falqui, A. Genovese, M. Allione, M. Moretti, S. Lopatin, L. Tirinato, G. Das, B. Torre, A. Giugni, F. Cesca, F. Benfenati, E. Di Fabrizio, *Nanoscale* **2017**, *9*, 2768.
[22] F. Gentile, M. Moretti, T. Limongi, A. Falqui, G. Bertoni, A. Scarpellini, S. Santoriello, L. Maragliano, R. Proietti Zaccaria, E. di Fabrizio, *Nano Lett.* **2012**, *12*, 6453.
[23] P. Zhang, M. Moretti, M. Allione, Y. Tian, J. Ordonez-Loza, D. Altamura, C. Giannini, B. Torre, G. Das, E. Li, S. T. Thoroddsen, S. M. Sarathy, I. Autiero, A. Giugni, F. Gentile, N. Malara, M. Marini, E. Di Fabrizio, *Commun. Biol.* **2020**, *3*, 457.
[24] M. Moretti, M. Allione, M. Marini, B. Torre, A. Giugni, T. Limongi, G. Das, E. Di Fabrizio, *Microelectro. Eng.* **2017**, *178*, 194.
[25] M. Moretti, M. Allione, M. Marini, A. Giugni, B. Torre, G. Das, E. Di Fabrizio, *Microelectron. Eng.* **2018**, *191*, 54.
[26] D. Matthies, C. Bae, G. E. S. Toombes, T. Fox, A. Bartesaghi, S. Subramaniam, K. J. Swartz, *eLife* **2018**, *7*, 37558.
[27] R. G. Efremov, C. Gatsogiannis, S. Raunser, *Methods Enzymol.* **2017**, *594*, 1.
[28] A. O. Oluwole, B. Danielczak, A. Meister, J. O. Babalola, C. Vargas, S. Keller, *Angew. Chem., Int. Ed. Engl.* **2017**, *56*, 1919.
[29] J. P. Renaud, A. Chari, C. Ciferri, W. T. Liu, H. W. Remigy, H. Stark, C. Wiesmann, *Nat. Rev. Drug Discovery* **2018**, *17*, 471.
[30] T. Nakane, A. Kotecha, A. Sente, G. McMullan, S. Masiulis, P. M. G. E. Brown, I. T. Grigoras, L. Malinauskaite, T. Malinauskas, J. Miehling, T. Uchański, L. Yu, D. Karia, E. V. Pechnikova, E. de Jong, J. Keizer, M. Bischoff, J. McCormack, P. Tiemeijer, S. W. Hardwick, D. Y. Chirgadze, G. Murshudov, A. R. Aricescu, S. H. W. Scheres, *Nature* **2020**, *587*, 152.
[31] B. Schreiber, D. Gkogkou, L. Dedelaite, J. Kerbusch, R. Hübner, E. Sheremet, D. R. T. Zahn, A. Ramanavicius, S. Facsko, R. D. Rodriguez, *RSC Adv.* **2018**, *8*, 22569.
[32] M. L. Coluccio, F. Gentile, G. Das, A. Nicastri, A. M. Perri, P. Candeloro, G. Perozziello, R. P. Zaccaria, J. S. T. Gongora, S. Alrasheed, A. Fratalocchi, T. Limongi, G. Cuda, E. D. Fabrizio, *Sci. Adv.* **2015**, *1*, 1500487.
[33] H. Altug, S.-H. Oh, S. A. Maier, J. Homola, *Nat. Nanotechnol.* **2022**, *17*, 5.
[34] M. Moretti, G. Das, B. Torre, M. Allione, E. Di Fabrizio, *Opt. Lasers Eng.* **2016**, *76*, 52.
[35] R. Intartaglia, S. Beke, M. Moretti, F. De Angelis, A. Diaspro, *Lab Chip* **2015**, *15*, 1343.
[36] G. Das, M. M, B. Torre, M. Allione, A. Giungi, E. D.i Fabrizio, *Biochem. Anal. Biochem.* **2017**, *6*.
[37] X. Qian, X.-H. Peng, D. O. Ansari, Q. Yin-Goen, G. Z. Chen, D. M. Shin, L. Yang, A. N. Young, M. D. Wang, S. Nie, *Nat. Biotechnol.* **2008**, *26*, 83.
[38] M. D. Hodges, J. G. Kelly, A. J. Bentley, S. Fogarty, I. I. Patel, F. L. Martin, N. J. Fullwood, *ACS Nano* **2011**, *5*, 9535.

[39] H. Ba, J. Rodríguez-Fernández, F. D. Stefani, J. Feldmann, *Nano Lett.* **2010**, *10*, 3006.
[40] S. H. W. Scheres, *J. Struct. Biol.* **2012**, *180*, 519.
[41] M. Li, Y. Yu, J. Yang, In *Transient Receptor Potential Channels*, (Ed: M. S. Islam), Springer Netherlands, Dordrecht **2011**; pp. 1–23.
[42] V. Y. Moiseenkova-Bell, L. A. Stanciu, I. I. Serysheva, B. J. Tobe, T. G. Wensel, *Proc. Natl. Acad. Sci.* **2008**, *105*, 7451.
[43] H. Shigematsu, T. Sokabe, R. Danev, M. Tominaga, K. Nagayama, *J. Biol. Chem.* **2010**, *285*, 11210.
[44] Y. Cheng, *Cell* **2015**, *161*, 450.
[45] Y. Z. Tan, P. R. Baldwin, J. H. Davis, J. R. Williamson, C. S. Potter, B. Carragher, D. Lyumkis, *Nat. Methods* **2017**, *14*, 793.
[46] T. Ravula, N. Z. Hardin, A. Ramamoorthy, *Chem. Phys. Lipids* **2019**, *219*, 45.
[47] V. Maingi, P. W. K. Rothemund, *ACS Nano* **2021**, *15*, 751.
[48] M. H. Chin, M. J. Mason, W. Xie, S. Volinia, M. Singer, C. Peterson, G. Ambartsumyan, O. Aimiuwu, L. Richter, J. Zhang, I. Khvorostov, V. Ott, M. Grunstein, N. Lavon, N. Benvenisty, C. M. Croce, A. T. Clark, T. Baxter, A. D. Pyle, M. A. Teitell, M. Pelegrini, K. Plath, W. E. Lowry, *Cell Stem Cell* **2009**, *5*, 111.
[49] G. T. Young, A. Gutteridge, H. D. E. Fox, A. L. Wilbrey, L. Cao, L. T. Cho, A. R. Brown, C. L. Benn, L. R. Kammonen, J. H. Friedman, M. Bictash, P. Whiting, J. G. Bilsland, E. B. Stevens, *Mol. Ther.* **2014**, *22*, 1530.
[50] S. Jiang, N. Wen, Z. Li, U. Dube, J. Del Aguila, J. Budde, R. Martinez, S. Hsu, M. V. Fernandez, N. J. Cairns, O. Harari, C. Cruchaga, C. M. Karch, *Transl. Psychiatry* **2018**, *8*, 265.
[51] J. Nagy, J. Kobolák, S. Berzsenyi, Z. Ábrahám, H. X. Avci, I. Bock, Z. Bekes, B. Hodoscsek, A. Chandrasekaran, A. Téglási, P. Dezső, B. Koványi, E. T. Vörös, L. Fodor, T. Szél, K. Németh, A. Balázs, A. Dinnyés, B. Lendvai, G. Lévay, V. Román, *Transl. Psychiatry* **2017**, *7*, 1179.
[52] Z. Nusser, *Curr. Opin. Neurobiol.* **2012**, *22*, 366.
[53] E. J. Akin, L. Solé, B. Johnson, M. E. Beheiry, J.-B. Masson, D. Krapf, M. M. Tamkun, *Biophys. J.* **2016**, *111*, 1235.
[54] C. Canale, B. Torre, D. Ricci, P. C. Braga, *Methods Mol. Biol.* **2011**, *736*, 31.
[55] S. Ahuja, S. Mukund, L. Deng, K. Khakh, E. Chang, H. Ho, S. Shriver, C. Young, S. Lin, J. P. Johnson Jr., P. Wu, J. Li, M. Coons, C. Tam, B. Brillantes, H. Sampang, K. Mortara, K. K. Bowman, K. R. Clark, A. Estevez, Z. Xie, H. Verschoof, M. Grimwood, C. Dehnhardt, J. C. Andrez, T. Focken, D. P. Sutherlin, B. S. Safina, M. A. Starovasnik, D. F. Ortwine, et al., *Science* **2015**, *350*, aac5464.
[56] R. García, R. Magerle, R. Perez, *Nat. Mater.* **2007**, *6*, 405.
[57] M. Stark, C. Möller, D. J. Müller, R. Guckenberger, *Biophys. J.* **2001**, *80*, 3009.
[58] S. Santos, N. H. Thomson, *Appl. Phys. Lett.* **2011**, *98*, 013101.
[59] D. Martinez-Martin, E. T. Herruzo, C. Dietz, J. Gomez-Herrero, R. Garcia, *Phys. Rev. Lett.* **2011**, *106*, 198101.
[60] J. Baniukevic, I. Hakki Boyaci, A. Goktug Bozkurt, U. Tamer, A. Ramanavicius, A. Ramanaviciene, *Biosens. Bioelectron.* **2013**, *43*, 281.
[61] E. Das, S. Alrasheed, A. Giugni, M. Allione, B. Torre, E. Di Fabrizio, M. L. Coluccio, G. Perozziello, P. Candeloro, *Nuovo Cimento Soc. Ital. Fis.* **2016**, *39*, 547.
[62] M. Moretti, R. Proietti Zaccaria, E. Descrovi, G. Das, M. Leoncini, C. Liberale, F. De Angelis, E. Di Fabrizio, *Plasmonics* **2013**, *8*, 25.
[63] F. Zolea, F. Biamonte, P. Candeloro, M. Di Sanzo, A. Cozzi, A. Di Vito, B. Quaresima, N. Lobello, F. Trecroci, E. Di Fabrizio, S. Levi, G. Cuda, F. Costanzo, *Free Radical Biol. Med.* **2015**, *89*, 614.
[64] S. Scalise, L. Scaramuzzino, V. Lucchino, C. Esposito, P. Malatesta, K. Grillone, N. Perrotti, G. Cuda, E. Immacolata Parrotta, *Stem Cell Res.* **2020**, 102083.
[65] V. Lucchino, L. Scaramuzzino, S. Scalise, K. Grillone, M. Lo Conte, C. Esposito, U. Aguglia, E. Ferlazzo, N. Perrotti, P. Malatesta, E. I. Parrotta, G. Cuda, *Stem Cell Res.* **2021**, *53*, 102329.
[66] M. T. De Angelis, E. I. Parrotta, G. Santamaria, G. Cuda, *Cell Death Dis.* **2018**, *9*, 6.
[67] F. J. Muller, B. M. Schuldt, R. Williams, D. Mason, G. Altun, E. P. Papapetrou, S. Danner, J. E. Goldmann, A. Herbst, N. O. Schmidt, J. B. Aldenhoff, L. C. Laurent, J. F. Loring, *Nat. Methods* **2011**, *8*, 315.
[68] F. De Angelis, F. Gentile, F. Mecarini, G. Das, M. Moretti, P. Candeloro, M. L. Coluccio, G. Cojoc, A. Accardo, C. Liberale, R. P. Zaccaria, G. Perozziello, L. Tirinato, A. Toma, G. Cuda, R. Cingolani, E. Di Fabrizio, *Nat. Photonics* **2011**, *5*, 682.
[69] E. F. Pettersen, T. D. Goddard, C. C. Huang, G. S. Couch, D. M. Greenblatt, E. C. Meng, T. E. Ferrin, *J. Comput. Chem.* **2004**, *25*, 1605.
[70] K. Zhang, *J. Struct. Biol.* **2016**, *193*, 1.
[71] S. Chen, G. McMullan, A. R. Faruqi, G. N. Murshudov, J. M. Short, S. H. W. Scheres, R. Henderson, *Ultramicroscopy* **2013**, *135*, 24.
[72] P. B. Rosenthal, R. Henderson, *J. Mol. Biol.* **2003**, *333*, 721.
[73] S. H. W. Scheres, S. Chen, *Nat. Methods* **2012**, *9*, 853.
[74] M. Y. Nurshazwani Muhamad Mahfuz, A. Zakiah, *IAES Intern. J. Artif. Intell.* **2019**, *8*, 7.
[75] F. Murtagh, P. Legendre, *J. Classification* **2014**, *31*, 274.
[76] D. Nečas, P. Klapetek, *Open Phys.* **2012**, *10*, 181.
[77] C. A. Schneider, W. S. Rasband, K. W. Eliceiri, *Nat. Methods* **2012**, *9*, 671.
[78] J. De Gelder, K. De Gussem, P. Vandenabeele, L. Moens, *J. Raman Spectrosc.* **2007**, *38*, 1133.